Central European Journal of Energetic Materials
ISSN 1733-7178; e-ISSN 2353-1843

Cent. Eur. J. Energ. Mater. 2021, *18*(3): 293-321; DOI 10.22211/cejem/140074
Article is available in PDF-format, in colour, at:
https://ipo.lukasiewicz.gov.pl/wydawnictwa/cejem-woluminy/vol-18-nr-3/

Research paper

Hemispherical Zirconium Liner for Advanced Shaped Charge with Enhanced Behind Armour Effect

Tamer Abd Elazim Elshenawy[1,*)], **Sherif Elbasuney**[2)]

[1)] *Technical Research Centre, Cairo, Egypt*
[2)] *Nanotechnology Research Centre, Military Technical College, Cairo, Egypt*
*E-mail: tamershenawy@yahoo.com

Abstract: Armour penetration is an essential outcome for shaped charges, especially when the behind-armour effect is considered. Hemispherical liners produce superior jet mass compared with those of traditional conical shape. In this paper two different materials have been studied as hemispherical shaped charge liners. The reference liner was hemispherical oxygen-free high-conductivity copper (OFHC); the other liner material was zirconium. These liners were experimentally tested against 4340 steel targets in shaped charges loaded with the same amount of Composition B explosive. Zirconium liners were found to offer superior performance with experimental penetration and crater diameter respectively 16% and 20% greater than OFHC. Ansys Autodyn hydrocode simulation results demonstrated that both liners produced superior jet masses exceeding 50% of the total liner mass. Moreover, zirconium had a jet tip velocity of 4869 m/s compared with 3886 m/s for OFHC. Additionally, zirconium had a superior average jet collapse to plastic deformation temperature ratio of 0.73 compared with 0.34 for OFHC. This is the first time the relation between the jet temperature during collapse and jet stretching has been reported.

Keywords: hollow charge, penetration, copper liner, zirconium liner, jet temperature

1 Introduction

Modern troops can be easily protected from fragmentation warheads using armoured vehicles. However, there is no effective protection against anti-armour shaped charges in either main battle tanks or light armoured vehicles. Shaped charge performance depends on various parameters including liner material, geometry, stand-off distance, and explosive charge; Figure 1.

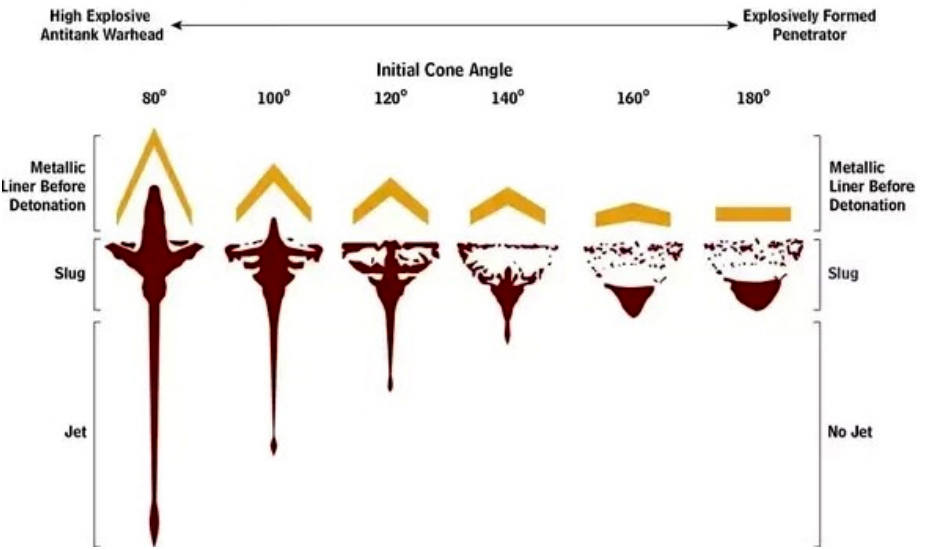

Figure 1. Jet and slug formation as a function of shaped charge angle

More recently, hemispherical liners have been attracting increasing attention as they can generate a high jet mass compared with the traditional conical shape. Therefore hemispherical liners could find wide application in advanced hollow charge applications against armoured vehicles. Such liners could be effective as the main liner for armour piercing shaped charges; Figure 2(a). They could also be effective as the tipping charge for Tandem warheads; Figure 2(b).

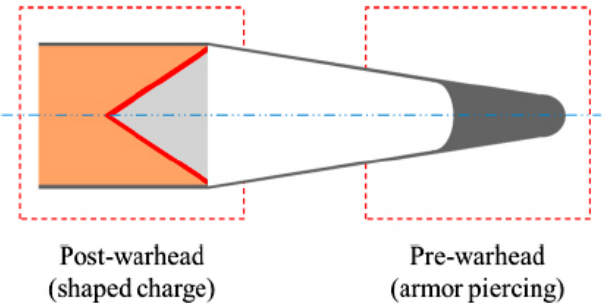

(a)

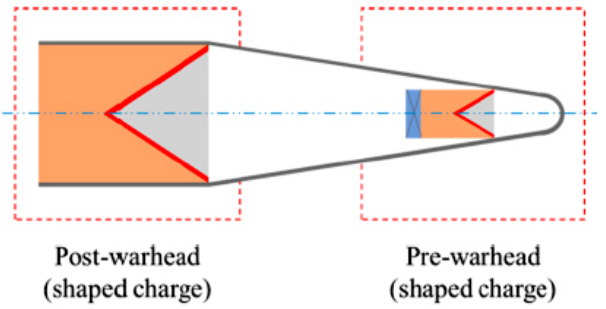

(b)

Figure 2. Schematic armour piercing shaped charges (a) single shaped charge, (b) (Tandem) warhead

Various materials have been employed as shaped charge liners [1]. In this application, zirconium, copper, silver, steel, titanium and depleted uranium have been studied due to their jet break-up time and effective jet length [2-4]. Glass has also been investigated as a liner material and exhibited a large breakup time in comparison with the traditional copper for large stand-off distances [3], but its low density compared to copper eliminates it for wide usage. Non-traditional metallic sheet liners such as pressed compacted powder liners were patented in 2001 by Reese and Hetz [5]. Stinson *et al.* [6] patented the methodology for producing single phase tungsten or molybdenum liners using the hot iso-static pressing technique. Walters *et al.* [7] have fired un-sintered copper tungsten liners against steel targets at short stand-off distances using the OMNI shaped charge. Halliburton Energy Services patented a number of different powder liners including tungsten, copper, lead, tantalum and molybdenum [8, 9]. Hemispherical liners can produce superior jets with larger

mass compared with the traditional conical shape and also lower off-axis drift velocities at extended stand-off distances [10].

This research is devoted to the design of precursor shaped charges with a high capability of achieving large perforation depth and a wide crater hole in an armoured body to boost the behind-armour effect caused by the main charge. In addition, pyrophoric zirconium liners were tested and compared to the baseline of copper as their shaped charges have been used independently to defeat light armoured vehicles. Zirconium could offer a large penetration depth due to its high ductility and cumulative jet length [2]. Additionally zirconium could be accompanied with an enhanced behind-armour incendiary effect due to its pyrophoric nature. Its stretching jet has been reported as reaching a high temperature [11]. Two different materials (zirconium and copper) were tested in hemispherical liners in precursor charges. Numerical modelling using the Ansys Autodyn hydrocode was performed to study the effect of liner properties on the coherency of the produced jets and their characteristics. The numerical hydrocode was also used to assess the temperature reached by jets of copper and zirconium and the accompanying behind-armour effect. The performance of these two liner materials was also assessed by static firing against 4340 steel targets, for which both the penetration depths and the crater diameters were measured. Zirconium liners gave 16% greater penetration and 20% greater crater diameter compared with oxygen-free high-conductivity copper (OFHC) in experimental penetration tests.

2 Experimental

2.1 Liner manufacture

The jet material is required to have high ductility in order to sustain long breakup times as well as enhanced coherent performance [12]. The baseline hemispherical liner was OFHC, grade C10100. This material has high purity (99.99%), low oxygen and phosphorus contents. C10100 has a minimum 101% IACS conductivity rating. The impurity percentages of the copper material employed are listed in Table 1. This copper is finished to a final form in a carefully regulated, oxygen-free environment.

Table 1. The elemental percentage of impurities in reference copper alloy C10100 grade material

Element	Impurities amount [%]
Cu	99.99*)
Pb	0.0005
Zn	0.0001
Fe	0.001
P	0.0003
Ag	0.0025
As	0.0005
O	0.0005
Sb	0.0004
Te	0.0002
Ni	0.001
S	0.0015
Se	0.0003
Bi	0.0001

*) The minimum copper content in this copper grade is ≥99.99% and is determined precisely by the difference between the total impurities and the 100% (according to the ASTM B152/B152M-09 standard for C10100)

On the other hand zirconium is an interesting material due to its long cumulative jet length and high ductility factors [2]. The raw material was a solid cylinder of pure zirconium 4N (99.9951) having a diameter of 46.17 mm and a length of 99.89 mm with a density of 6623 kg/m^3. The impurity percentages of the zirconium material employed are listed in Table 2.

Table 2. The elemental percentage of impurities in the zirconium material

Element	Impurities [wt.%]
Fe	0.005
Cr	0.0009
C	0.001
N	0.008

Zirconium rod was annealed at 900 °C for 1 h in order to obtain a relative small average grain size. This process improves its ductility and breakup time, thereby improving its performance as a liner material [13]. Copper and zirconium liners were manufactured by a turning technique using a high precision CNC machine (5 μm precision) (Figure 3).

Figure 3. The manufactured zirconium (left) and copper (right) liners

Composition B composed of 60/40 RDX/TNT by weight was used in the shaped charges. Composition B was developed by melting TNT in a steam-jacketed kettle; RDX was then added slowly with stirring. Composition B has a detonation velocity of 8027 m/s, and a density of 1590 kg/m^3 [14]. Table 3 summarizes the main explosive properties of Composition B.

Table 3. The detonation characteristics of the explosive used

Sample	Loading density [kg/m^3]	Detonation velocity [m/s]	Detonation pressure [kPa]	Heat of detonation [kJ/m^3]
Composition B	1620	7836	$2.40 \cdot 10^7$	$9.204 \cdot 10^6$

Shaped charges were loaded with 50 g of Composition B. They were then attached to AISI 4340 steel targets which had been annealed at 810 ºC to give them a yield strength of 470 MPa. Two different stand-off distances (80 and 100 mm) were employed (see Figure 4). These stand-off distances were evaluated using Autodyn hydrocode so as to maintain continuous jet penetration during crater formation.

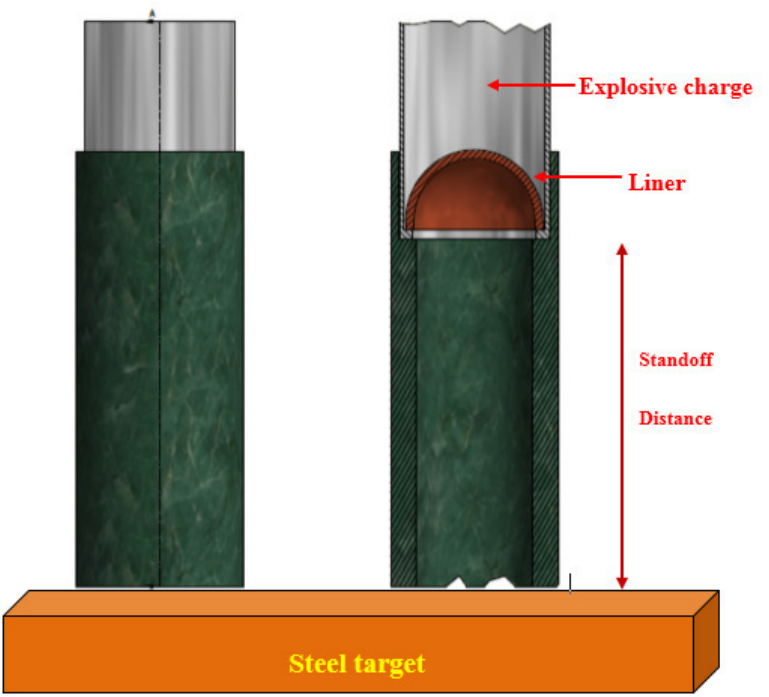

Figure 4. The experimental penetration test setup

3 Numerical Calculations

3. 1 Autodyn numerical hydrocode

Three different schemes including jetting analysis, jet formation, and jet interaction with the steel target (penetration) were implemented. The jetting analysis (based on unsteady state PER theory) was employed to the calculate the masses and velocities of the jet and slug, as well as the resultant kinetic energy and jet momentum [15]. The collapse, flow and jet velocities, the liner collapse, deflection angles, and jet kinetic energy were also estimated. The jet radius and elemental break-up time were estimated based on the output standard jetting analysis [15]. Jet formation was performed using an Euler solver based on continuum mechanics to obtain the jet profiles at different times (s) [16]. The output of this scheme (jet having a certain momentum at certain time) was employed as the input of a Lagrange-Lagrange jet-target interaction scheme.

Jet penetration of the steel target was modeled using the Lagrange method. In this scheme, the obtained jet was remapped to Lagrangian moving grids and impacted the steel target. The overall crater profile inside the steel target could be monitored. Further details such as erosion strain effect and mesh sensitivity analysis as well as the validity and verification of reference [17].

3.2 Material model

The equation of state (EOS) for the high explosive employed is the Jones-Wilkins-Lee (JWL) equation. The experimental constants for the explosives employed were determined from sideways plate push dynamic test experiments [18] and the cylinder expansion test [19-21]. The Composition B explosive loading density was 1.62 g/cm^3. The parameters A, B, ω, R_1, and R_2 in the JWL EOS equation were 8.1658 · 10^8 kPa, 1.6228 · 10^7 kPa, 0.185, 4.067, and 1.377, respectively. The detonation velocity was 7836 m/s, and the detonation pressure was 2.40 · 10^7 kPa. The C-J energy per unit volume was 9.204 · 10^6 kJ/m^3. The copper liner material had a density of 8.9 g/cm^3. Copper was modeled using a linear EOS with bulk modulus 1.0 · 10^8 kPa and a reference temperature of 293 K. The strength model used was Johnson-Cook (J-C) (Equation 1).

$$\sigma = (A + B\varepsilon^n)(1 + Cln\dot{\varepsilon}^*)(1 - T_H^m) \tag{1}$$

where σ, ε, A, B, n, C, and m are dynamic flow stress, effective plastic strain, yield strength, hardening constant, hardening exponent, strain-rate constant, and thermal exponent constant, respectively. $\dot{\varepsilon}^*$ is the normalized effective plastic strain-rate (*i.e.* the applied true strain-rate divided by the reference strain-rate). T_H is the homologous temperature that can be calculated using Equation 2.

$$T_H = \frac{T - T_{room}}{T_{melt} - T_{room}} \tag{2}$$

where T_{room}, T_{melt} are room temperature and melting temperature, respectively. The J-C constants for the copper and zirconium materials are listed in Table 4.

Table 4. The material model and the mechanical properties of the liner materials used

Parameter	Unit	Material	
		Zirconium	Copper
Reference density	[g/cm^3]	6.623	8.93
A	[MPa]	170	90
B	[MPa]	450	292
n	–	0.6	0.31
C	–	0.01	0.025
m	–	0.5	1.09
$\dot{\varepsilon}_o$	[1/s]	$8 \cdot 10^{-5}$	1
Parameter C	[m/s]	3296	3958
Parameter S	–	1.271	1.497
Reference temperature	[K]	300	300

The explosive charge case was polyvinyl chloride (PVC) of 0.915 g/cm^3 density with shock EOS parameters $C = 2901$ m/s and $S = 1.481$. The steel target material had a density of 7.86 g/cm^3 and shock EOS parameters Gruneisen coefficient 1.67 and parameters $C = 4397$ m/s and $S = 1.73$. The strength model employed for the steel target was the von Mises criterion of shear modulus 74 GPa, and yield stress of 470 MPa. The material parameters of the target are listed in Table 5.

Table 5. Properties of casing, and steel target materials [16]

Parameter	Unit	Material	
		PVC	Steel Targets Hardness; HB 217
Equation of state	–	Shock	
Reference density	[g/cm^3]	0.915	7.86
Gruneisen coefficient	–	1.64	1.67
Parameter C	[m/s]	2901	4397
Parameter S	–	1.481	1.73
Reference temperature	[K]	300	
Strength model	–	–	von Mises
Shear modulous	[GPa]	–	74
Yield strength	[MPa]	–	470

4 Results and Discussion

4.1 Numerical shaped charge jetting analysis

Jet velocity-cumulative jet mass for the two liner materials (copper and zirconium) were obtained using a numerical shaped charge jetting analysis. Even though the two liners had the same wall thickness of 2 mm, the jet collapse velocities produced are different, and therefore the flow velocity, the stagnation velocity as well as their jet velocity are different. Whereas the copper liner exhibited a maximum jet tip velocity of 3886 m/s, that for zirconium was 4869 m/s. While the cumulative jet mass in the case of the copper liner was 52% of the total liner mass, zirconium produced a faster jet with 55% of the total liner mass (Figure 5).

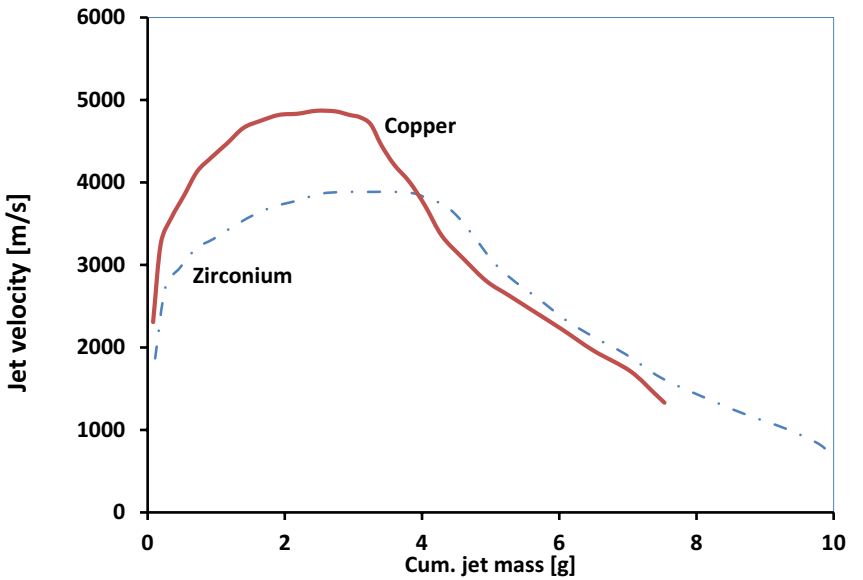

Figure 5. The jet velocity-cumulative jet mass for the two liner materials studied

The maximum flow velocity was found to be 1786 and 2222 m/s for the copper and zirconium liners, respectively. These values were found to be much lower than the limits of the coherent jet values of 4846 m/s for copper and 4054 m/s for zirconium [22]. Figures 6 and 7 shows the sequence of the jet formation in both liners as well as jet stretching up to time 31 μs.

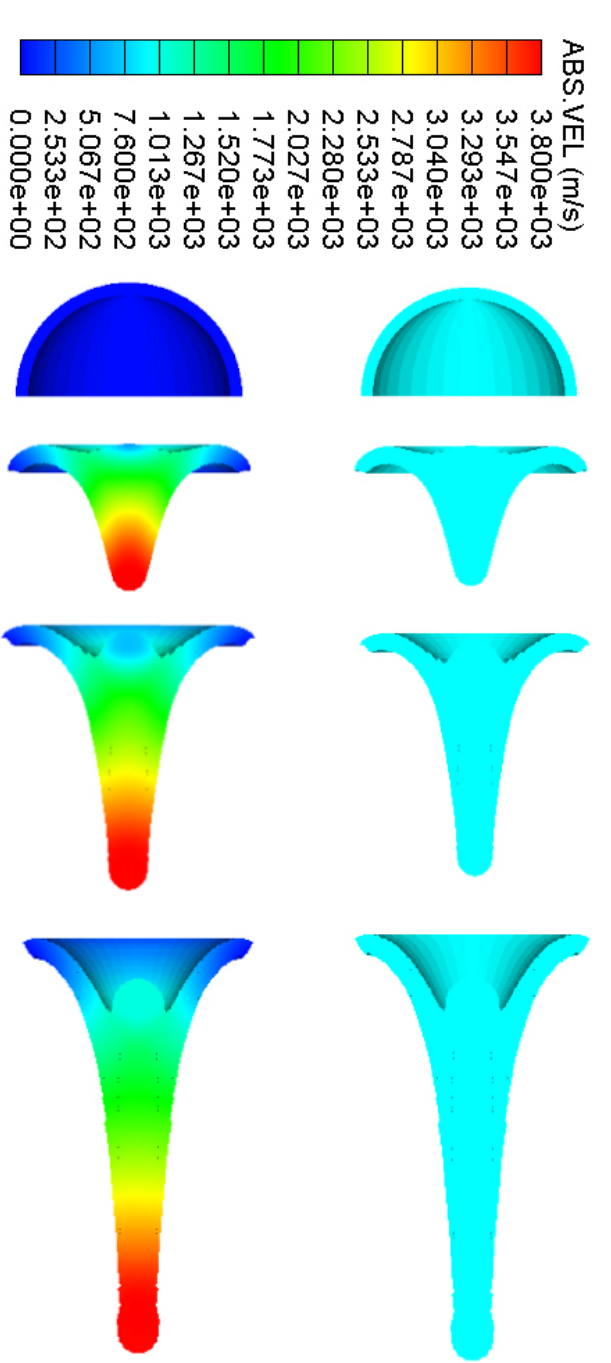

Figure 6. The copper jet profile and its velocity at 0, 20, 28, and 38 μs

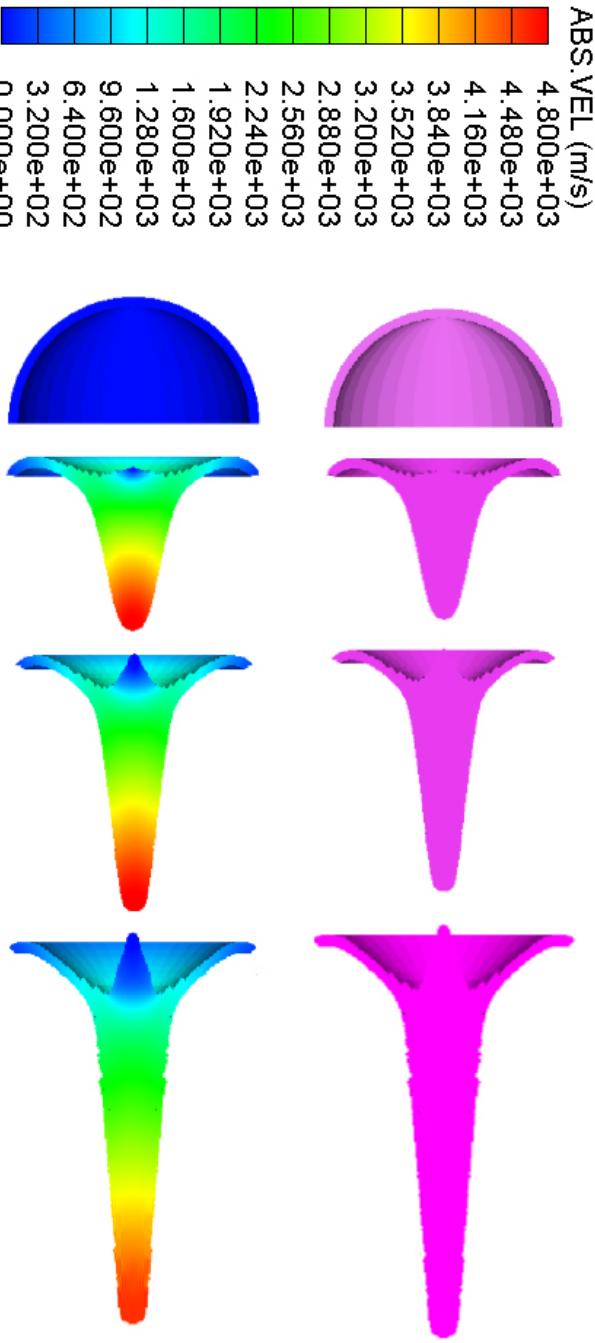

Figure 7. The zirconium jet profile and its velocity at 15.3, 25.7, and 31.1 μs

The copper jet demonstrated a lower velocity than zirconium. This could be ascribed to its higher density. Consequently it has a higher resistance to plastic deformation compared with zirconium.

HTML post processing data for the jetting analysis was used for further calculations in the two cases to estimate the jet radius and the breakup time for both liners. The breakup time (t_b) was calculated based on the simple Hirsch equation using Equation 3.

$$t_b = \frac{2r}{V_{PL}} \tag{3}$$

where r is the initial radius of the jet element when the jet has just formed (Equation 4).

$$r = \sqrt{2RT_L}\sin\left(\frac{\beta}{2}\right) \tag{4}$$

where R, β are the initial inner radius of the liner element and elemental collapse angle of the liner element, respectively.

4.2 Jet velocity – breakup times

V_{PL} is a characteristic plastic velocity representing the average velocity difference between the neighboring jet segments. The reciprocal of V_{PL} ($1/V_{PL}$) represents the specific breakup time for liner materials. It has been found to scale linearly with the (T_L/C_D) values for the zirconium material, the scaling being described by Elshenawy *et al.* [3] in the following Equation 5:

$$\frac{1}{V_{PL}} = 15.71 - 16.169\left(\frac{T_L}{C_D}\right) \tag{5}$$

which is similar to that proposed by Hirsch [23] for the copper liner material, which is

$$\frac{1}{V_{PL}} = 13.886 - 101.149\left(\frac{T_L}{C_D}\right) \tag{6}$$

where (T_L/C_D) is the liner thickness scaled to the charge diameter.

Elemental breakup time calculations showed an average breakup time of 125 μs in the case of zirconium, by comparison with 64 μs in the case of the copper jet (Figure 8).

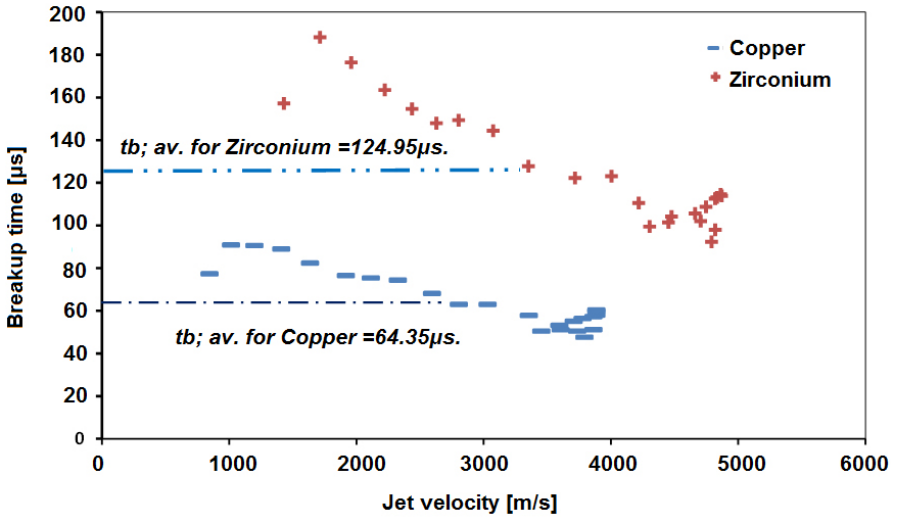

Figure 8. The jet velocity-breakup times for both copper and zirconium charges

The enhanced break up times for zirconium could be ascribed to the enhanced jet radius as well as an enhanced characteristic plastic velocity. This can offer superior performance for zirconium liners compared with traditional OFHC. Table 6 summarize the main jetting parameters of the hemispherical zirconium liner compared to traditional OFHC.

Table 6. The jetting calculation outputs for the baseline copper and the zirconium

Parameter	Unit	Material	
		Copper	Zirconium
Liner mass	[g]	28.6	20.7
Jet mass	[g]	14.9	11.30
Jet percentage	[%]	52	55
Jet kinetic energy	[kJ]	17.3	20.0
Maximum jet tip velocity	[m/s]	3886	4869
Maximum flow velocity	[m/s]	1786	2222

4.3 Crater formation

The remapped jets from Euler solvers were allowed to impact steel 4340 targets, the total penetration depth being calculated either when the jet is totally consumed on the crater walls or when its velocity falls below a certain value (termed the cut-off element). The penetration craters for both liners are represented in Figure 9, for copper and zirconium liners.

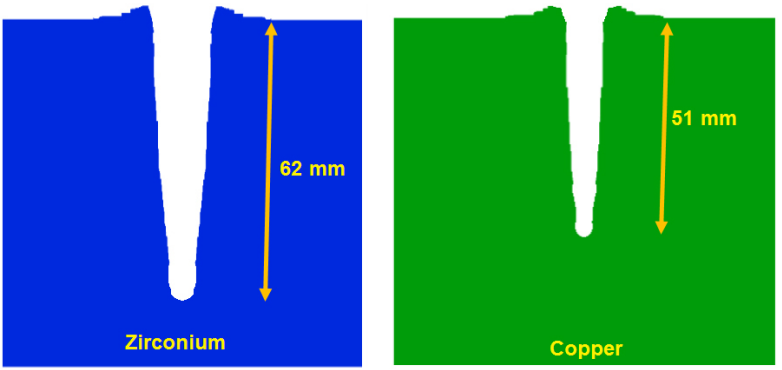

Figure 9. The numerical crater profile inside steel targets for copper and zirconium liners

While the copper liner exhibited a penetration depth of 51 mm, the zirconium liner achieved a larger penetration depth of 62 mm. Additionally, zirconium offered an enhanced crater profile with a larger volume compared with OFHC (Figure 10). This may be attributed to the high velocity obtained by the zirconium jet. The emphasized penetration crater was achieved and found sufficient to perforate armoured vehicles. One more factor that should be considered is machining safety during manufacturing of the zirconium liner. All these parameters should be optimized in order to choose a final optimum liner design in general and the liner material specifically.

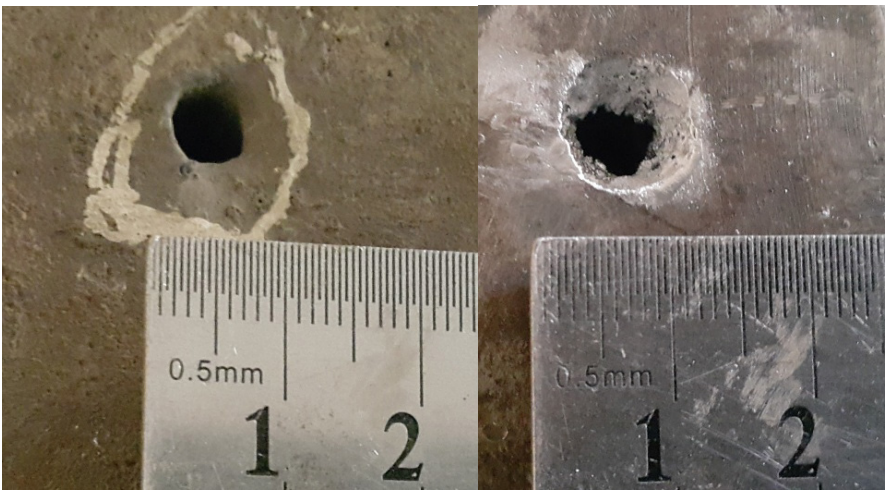

Figure 10. The penetrated steel targets for copper (left) and zirconium (right) targets

4.4 Crater growth calculations

Since the crater radius is our goal, the crater was estimated using Held's formula [24], where the crater radius as a function of time was estimated using the jet parametric data obtained from the jetting analysis and target resistance to plastic deformation (Equation 7).

$$r_c(\mathrm{t}) = \sqrt{\frac{A}{B} - \left(\sqrt{\frac{A}{B} - r_j^2} - t\sqrt{B}\right)^2} \tag{7}$$

with constants A and B defined as

$$A = \frac{r_j^2 V_j^2}{\left(1+\sqrt{\frac{\rho_t}{\rho_j}}\right)^2} \tag{8}$$

$$B = 2\frac{R_t}{\rho_t} \tag{9}$$

where ρ_t, ρ_j, t, V_j, r_j, and R_t are respectively the target and jet densities, time, jet tip velocity, jet radius, and target strength. Target strength (resistance to penetration) can be defined by Equation 10.

$$R_t = AY_t\left(1 + B\ln\frac{2E}{3Y_t}\right) \tag{10}$$

where E is the Young's modulus and Y_t is the target yield strength [25]. It was found that $A = 1.38$ and $B = 0.73$ for a cavity expansion model using best data fitting optimization [26], and thus, Equation 10 has the form

$$R_t = 1.38Y_t\left(1 + 0.73\ln\frac{2E}{3Y_t}\right) \tag{11}$$

Based on the previous equations, the maximum crater radius (r_{cm}) could be estimated by

$$r_{cm} = \sqrt{\frac{A}{B}} \tag{12}$$

The final calculated crater times based on the above equation were found to be 6.78 and 8.44 μs for copper and zirconium jets, respectively. On the other hand, the crater radius calculations were found to be 7.1 and 8.5 mm for the copper and zirconium jets, respectively. The main reason behind the difference between the calculated and experimental values of the crater radius was found to be the target strength value: the target strength (R_t) was taken to be 3.33 GPa [26]. Figure 11 shows the crater evolution with time for both copper and zirconium jets.

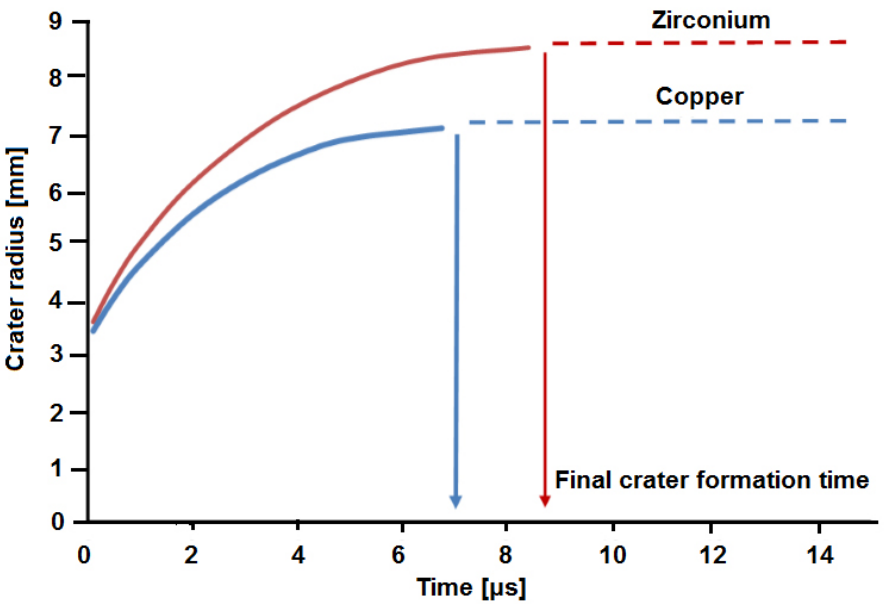

Figure 11. Crater development with time for both copper and zirconium jets

Penetration depth calculations were conducted using a modified virtual origin (VO) model [26]. The target strength effect on the penetration reduction was not considered. The equation of the continuous jet is represented by Equation 13.

$$P = Z_0\left[\left(\frac{V_0}{V_c}\right)^{\frac{1}{\gamma}} - 1\right]\left(1 - \lambda\frac{R_t}{\rho_j {V_C}^2}\right) \qquad \text{for } 0 \le Z_0 < V_c t_b \left(\frac{V_c}{V_o}\right)^{\frac{1}{\gamma}} \tag{13}$$

where:

– Z_o is the effective jet length measured from the VO to the target surface,

– V_o and V_C are the jet tip and cut-off velocities, respectively,
– γ is the square root of the target-jet density ratio, *i.e.* $\gamma = \sqrt{\rho_T / \rho_j}$,
– λ is a constant determined from real experiments, which was found to be 200.31 from the average of four experimental tests using concrete targets.

The corrected prediction showed good agreement with experimental results [17]. On the other hand, Elshenawy *et al.* [26] reported that target yield strength was considered for the estimation of λ as follows:

$$\lambda = 0.8322 Y_t + 0.6122 \tag{14}$$

where Y_t is in GPa for AISI 4340 steel target, and $Y_t = 0.47$ GPa. For $Y_t = 0.47$ Pa, λ approximately equals 1. Figure 12 demonstrates the stand-off distance and the location of the VO point inside the liner.

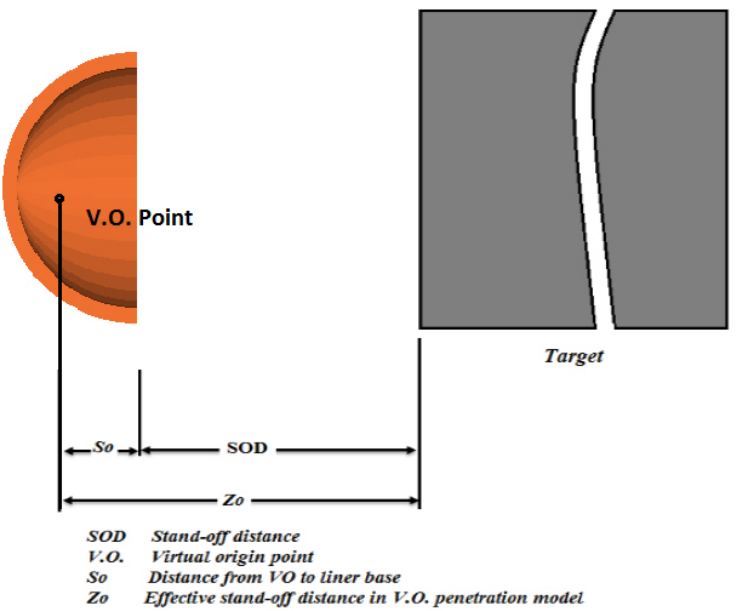

Figure 12. The location of the VO point and the VO stand-off model parameters

The real location of the VO point and the distance to the liner base is represented in Figure 13 for copper liners using the same approximation as used by Agu *et al.* [27]. Considering the numerical data obtained from the standard jetting analysis, a similar curve was developed for zirconium shaped-charge liners. The VO point was found to be 5.03 mm from the liner base for zirconium as compared to 4.47 mm in the case of copper.

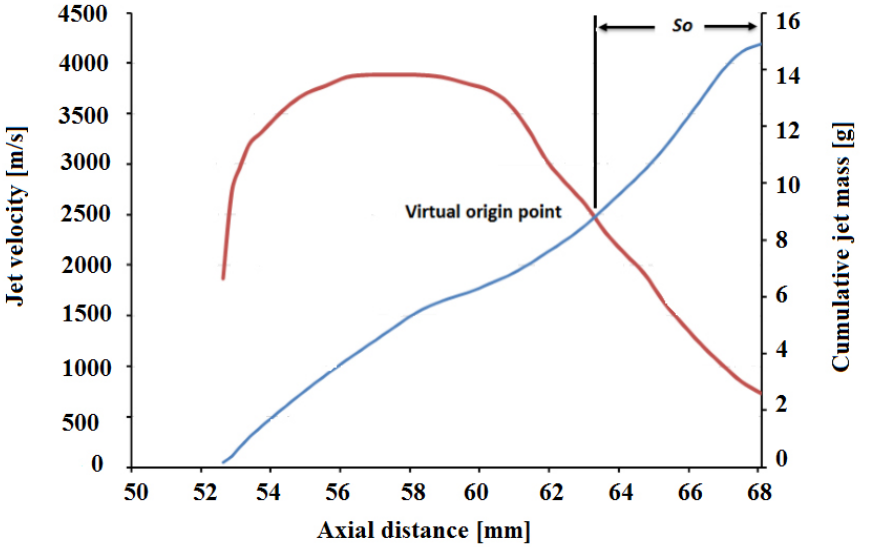

Figure 13. The determination of the VO location for copper shaped charge

Table 7 shows the shaped charge jet characteristics, the target materials, penetration corrections and penetration calculation parameters for the two shaped charges with copper and zirconium liners. Both charges were tested against steel target material grade AISI 4340 of hardness 217 HB.

Table 7. The calculated penetration parameters for copper and zirconium shaped charges

Parameter	Unit	Material	
		Copper	Zirconium
Target Yield strength	[GPa]	0.470	0.470
ρ_T	[kg/m^3]	7800	7800
ρ_j	[kg/m^3]	8900	6510
γ	–	0.94	1.09
Z_0	[mm]	84.47	105.03
V_j	[m/s]	3886	4869
V_c	[m/s]	2327	2728
Break-up time t_b	[ms]	0.0640	0.125
P-ideal[a)]	[cm]	6.16	7.33
$V_c t_b \left(\frac{V_c}{V_o}\right)^{\frac{1}{\gamma}}$	–	86	201
P-Exp.[b)]	[cm]	5.64	6.53
P*-Num.[c)]	[cm]	5.1	6.2
Reduction[d)]	[cm]	0.52	0.80
E_t	[GPa]	205	205
R_t	[GPa]	3.33	3.33
$R_t/\rho_j V_c^2$	–	0.069	0.069
λ(Eq (14))	–	1.00	1.00
$\lambda R_t/\rho_j V_c^2$	–	0.069	0.074
P-Ana[e)]	[cm]	5.73	6.82
Error[f)]	[%]	–1.59	–4.44

[a)] *P-Ideal: ideal penetration calculated using Equation 13 without strength correction term.*
[b)] *P-Exp.: experimental penetration depth.*
[c)] *Numerical penetration depth calculated using Autodyn hydrocode.*
[d)] *Reduction = (P-ideal) – (P-Exp.)*
[e)] *P-Ana : the penetration depth using Equation 13 considering target resistance and correction term.*
[f)] *Error % = ((P-Exp.) – (Penetration))/(P-Exp.) · 100, where (Penetration) is taken from Equation 13.*

Table 7 shows that zirconium liners achieve about a 16% greater experimental penetration depth into steel targets than baseline copper ones. The main reasons behind this result could be the change in the jet characteristics such as jet tip velocity, cut-off velocity, and the effective stand-off distance (Z_0). Table 7 also confirms that the classical VO model overpredicts the penetration depth, which was corrected by the target strength correction term that reduced the penetration depth with ratios about 7% and 7.5% for copper and zirconium liners, respectively.

4.5 Jet temperature calculation

The overall behind-armour effects for a shaped charge jet were summarized by Held [28] and reported as being spalls, heat, light, noxious fumes, smoke, blast and incendiary effects in addition to residual jet material. The residual jet material and the incendiary heat effects of zirconium were studied as part of further consideration of enhanced behind-armour effects of zirconium jets [1]. Arabei *et al.* [29] stated that zirconium bursts into bright flames at 420 °C in addition to its pyrophoric nature. Thus, the heating of shaped charge jets during plastic deformation is an important issue to be studied numerically due to the difficulty in making measurements experimentally. Three different mechanisms could withstand jet heating including liner grazing by the detonation wave of the explosive, the heating of the liner during its collapse process, and heating due to plastic deformation during jet stretching. It has been found that the third mechanism is the predominant one and has the largest impact on jet heating [11]. Thus, the Autodyn hydrocode was employed to investigate jet heating during shaped charge jet formation using the Mie-Gruneisen thermodynamic model based on the shock equation of state for both the copper and zirconium liners [3].

To verify the Autodyn jet temperature calculations during liner collapse and jet stretching, jet temperature calculations were compared to the measured values. The results were quite similar [30]. In an attempt to calculate the temperature of the jet, a few gauge points were assigned within the liner elements to investigate the temperature around the circumference of the jet core. These gauge points were also added to copper liners to check the jet temperature for comparison. The locations of the selected gauge points are represented in Figures 14 and 16 for zirconium and copper jets, respectively. Figures 15 and 17 show similar behaviour of jet heating starting from time 0 as well as during the stretching phase, until it reaches steady state. Figures 14 and 16 show similar contours and temperature variation for both copper and zirconium jets. It can be seen that the temperature varies across the width of the jet. The highest temperature was found at the inner core of the jet, decreasing gradually towards the outer surface.

The first peak represented in Figures 15 and 17 was attributed to jet heating during the collapse of the liner element until reaching steady state condition. In order to quantify the contributions of both of the two mechanisms *(i)* liner heating during the collapse process and subsequent jet stretching and *(ii)* plastic deformation, the maximum temperature was recorded for each gauge point separately and listed in Table 8 for the two liner materials studied.

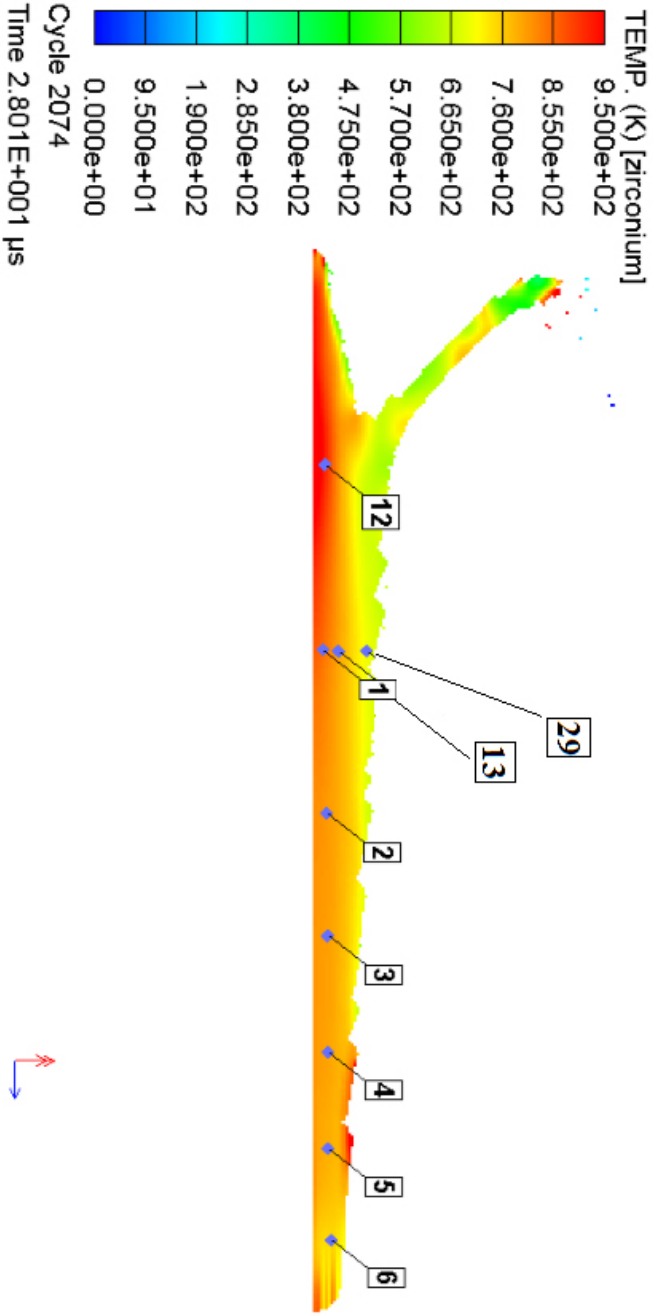

Figure 14. The locations of the moving gauge points inside the zirconium jet

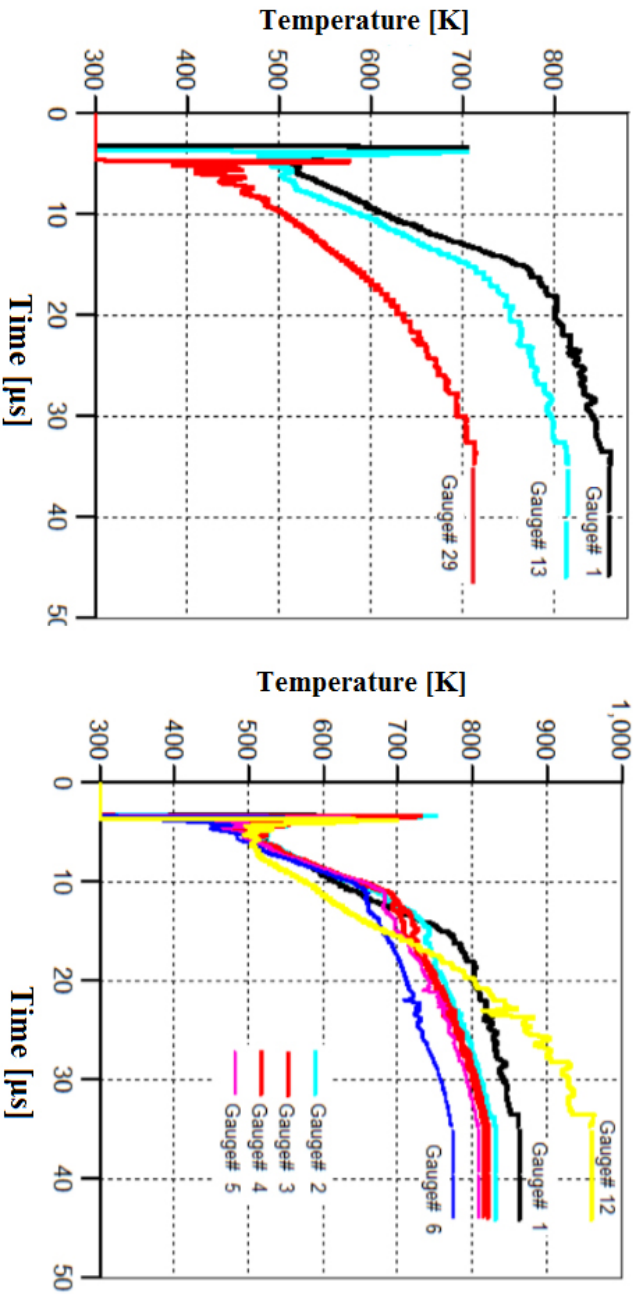

Figure 15. The calculated temperature along the jet length and its circumference for the zirconium liner

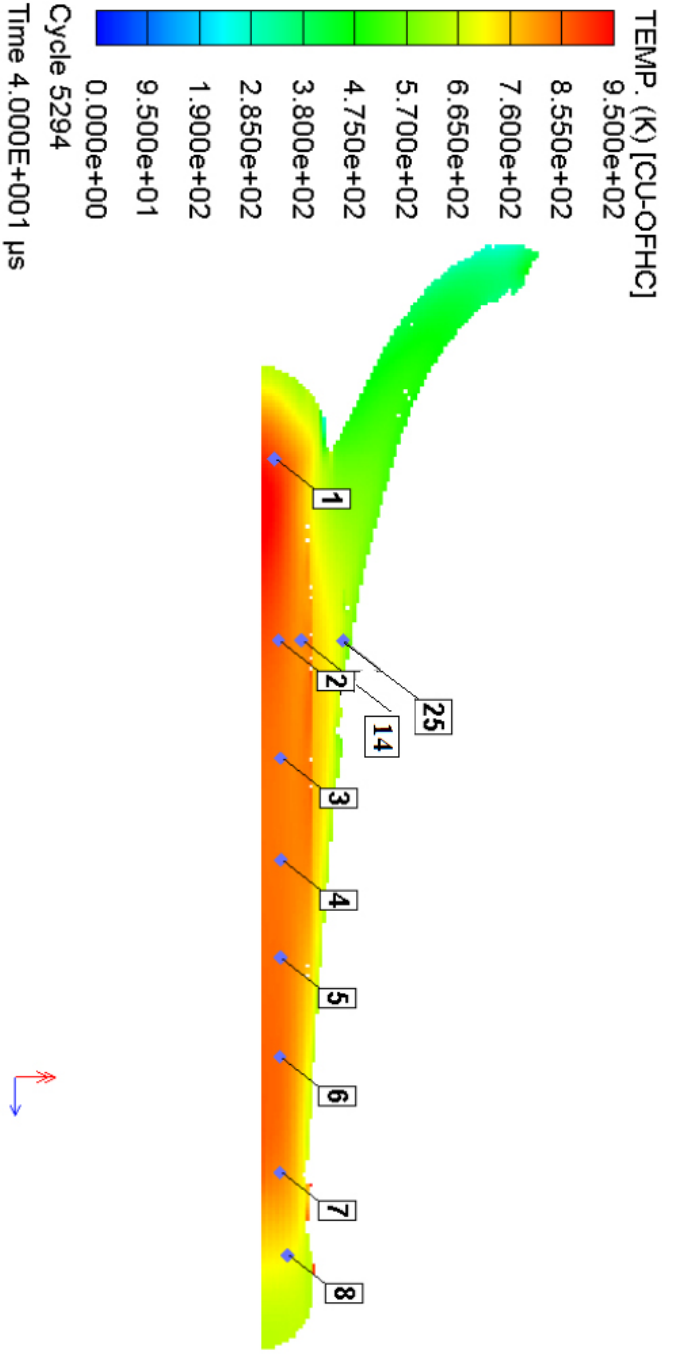

Figure 16. The locations of the moving gauge points inside the copper jet

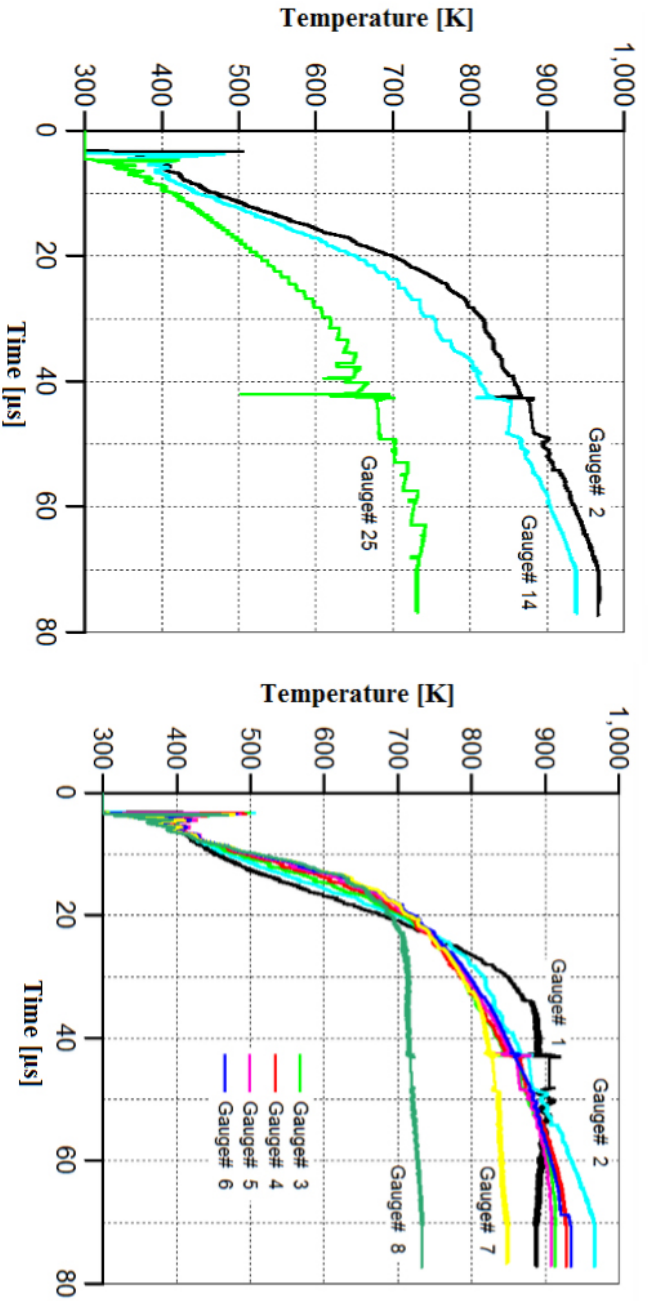

Figure 17. The calculated temperature along the jet length and its circumference for the copper liner

Table 8. The summary of the collapse and plastic deformation (Plast. Def.) heating temperatures for copper and zirconium jets

Zirconium jet				Copper jet			
Gauge	T-Collapse [°C]	T-Plast. Def. [°C]	T-Collapse/ (T-Plast. Def.)	Gauge	T-Collapse [°C]	T-Plast. Def. [°C]	T-Collapse/ (T-Plast. Def.)
1	433	590.2	0.73	1	231	646.8	0.36
2	477	558.5	0.85	2	232	694.5	0.33
3	459	548.8	0.84	3	225	641.4	0.35
4	426	542.7	0.78	4	220	655.3	0.34
5	363	534.4	0.68	5	212	636.3	0.33
6	273	498.7	0.55	6	207	661.6	0.31
12	426	691.0	0.62	7	205	576.1	0.36
13	433	542.3	0.80	8	196	461.4	0.42
29	304	442.0	0.69	14	205	666.3	0.31
				25	147	469.5	0.31

It can be concluded from Table 8 that most of the gauges show a ratio between the liner collapse temperature to the plastic deformation temperature of 0.55 to 0.85 with an average value of 0.73 for the zirconium liner. Copper exhibits lower values of the ratio (between 0.31 to 0.42) with an average value of 0.34. This difference between the copper and zirconium jets may be caused by the difference in the jet velocities in the two cases. This could result in different strain rates and therefore different values for the corresponding temperature in both mechanisms of jet or liner heating. Generally, most of the jet elements in the case of the copper liner exhibit higher temperatures than those in the zirconium liners, but the pyrophoric nature of the zirconium liner and the destructive behind-armour effects make the zirconium liner a higher priority to the traditional copper one.

5 Conclusions

- Two different shaped charges with copper and zirconium as liners have been suggested as precursor shaped charges.
- Relevant analysis for both shaped charges has revealed that zirconium liners can achieve 16% greater penetration depths compared to traditional copper ones. Besides, calculated radial crater analysis and verified experiments showed that the zirconium liner material also produces a 20% greater crater diameter. Additionally, numerical calculations of jet temperature

showed that copper liners have a higher temperature during jet formation than zirconium ones, but zirconium is preferred for its pyrophoric nature and behind-armour incendiary effect. Therefore it is recommended as a precursor charge for direct attack mode missiles.

- Numerical analysis showed that the average ratio between the collapse temperature and the plastic deformation temperature during jet stretching was found to be 0.73 for zirconium jets and 0.34 for copper jets.

References

[1] Buc, S.M. *Shaped Charge Liner Materials: Resources, Processes, Properties, Costs, and Applications*. Final Technical Report AD-A278 191, **1991**.

[2] Bourne, B.; Cowan, K.G.; Curtis, J.P. Shaped Charge Warheads Containing Low Melt Energy Metal Liners. *Proc. 19th Int. Symp. Ballistics*, Interlaken, Switzerland, **2001**, pp. 583-590.

[3] Elshenawy, T.; Li, Q.M. Breakup Time of Zirconium Shaped Charge Jet. *Propellants Explos., Pyrotech.* **2013**, *38*(5): 703-708.

[4] Elshenawy, T. Determination of the Velocity Difference between Jet Fragments for a Range of Copper Liners with Different Small Grain Sizes. *Propellants Explos., Pyrotech.* **2016**, *41*(1): 69-75.

[5] Reese, J.W.; Hetz, A. *Coated Metal Particles to Enhance Oil Field Shaped Charge Performance*. Patent US 7011027, **2006**.

[6] Stinson, J.S.; Nelson, S.R.; Wittman, C.L. *Method for Producing High Density Refractory Metal Warhead Liners from Single Phase Materials*. Patent US 5523048, **1996**.

[7] Walters, W.; Peregino, P.; Summers, R.; Leidel, D. *A Study of Jets from Unsintered Powder Metal Lined Non Precision Small Caliber Shaped Charge*. Army Research Laboratory Aberdeen Proving Ground, MD, Report ARL-TR-2391, **2001**.

[8] Zhang, X.; Wu, C.; Huang, F. Penetration of Shaped Charge Jets with Tungsten-Copper and Copper Liners at the same Explosive-to-Liner Mass Ratio into Water. *Shock Waves* **2010**, *20*(3): 263-267.

[9] Glenn, L.A. *Pressure Enhanced Penetration with Shaped Charge Perforators*. Patent US 6223656, **2001**.

[10] Whelan, A.J.; Furnisss, D.R.; Townsley, R.G. Experimental and Simulated (Analytical and Numerical) Elliptical-Form Shaped Charges. *Proc. 20th Int. Symp. Ballistics,* Orlando, Florida, **2002**, pp. 446-453.

[11] Racah, E. Shaped Charge Jet Heating. *Propellants Explos., Pyrotech.* **1988**, *13*(6): 178-182.

[12] Schwartz, A.; Kumar, M.; Lassila, D. Analysis of Intergranular Impurity Concentration and the Effects on the Ductility of Copper-Shaped Charge Jets. *Metall. Mater. Trans. A* **2004**, *35*(9): 2567-2573.

[13] Nielsen, R.H.; Wilfing, G. Zirconium and Zirconium Compounds. In: *Ullmann's Encyclopedia of Industrial Chemistry*, Willey VCH, **2012**; ISBN 3-527-20102-5, pp. 753.
[14] Chick, M.C.; Learmonth, L.A. *Determination of Shock Initiation and Detonation Characteristics of PE4 in Proof Test Geometries.* Materials Research Labs, Ascot Vale, Australia, Report MRL-R-979, **1985**.
[15] Pugh, E.M.; Eichelberger, R.J.; Rostoker, N. Theory of Jet Formation by Charges with Lined Conical Cavities. *J. Appl. Phys.* **1952**, *23*(5): 532-536.
[16] Cowler, M.S. *Autodyn Theory Manual*. Century Dynamics, CA, **1997**.
[17] Elshenawy, T.; Li, Q.M. Influences of Target Strength and Confinement on the Penetration Depth of an Oil Well Perforator. *Int. J. Impact Eng.* **2013**, *54*: 130-137.
[18] Tarver, C.M.; Tao, W.C.; Lee, C.G. Sideways Plate Push Test for Detonating Solid Explosives. *Propellants Explos., Pyrotech.* **1996**, *21*(5): 238-246.
[19] Lan, I.F.; Hung, S.C.; Chen, C.Y.; Niu, Y.M.; Shiuan, J.H. An Improved Simple Method of Deducing JWL Parameters from Cylinder Expansion Test. *Propellants Explos., Pyrotech.* **1993**, *18*(1): 18-24.
[20] Elek, P.M.; Džingalaševič, V.V.; Jaramaz, S.S.; Mickovič, D.M. Determination of Detonation Products Equation of State From Cylinder Test: Analytical Model and Numerical Analysis. *Therm. Sci.* **2015**, *19*(1): 35-48.
[21] Kato, H.; Kaga, N.; Takizuka, M.; Hamashima, H.; Itoh, S. Research on the JWL Parameters of Several Kinds of Explosives. Materials Science Forum. *Mater. Sci. Forum* **2004**, *465*: 271-276.
[22] Hasenberg, D. *Consequences of Coaxial Jet Penetration Performance and Shaped Charge Design Criteria*. Naval Postgraduate School, Monterey, CA, Report NPS-PH-10-001, **2010**.
[23] Hirsch, E. Scaling of the Shaped Charge Jet Break Up Time. *Propellants Explos., Pyrotech.* **2006**, *31*(3): 230-233.
[24] Held, M.; Kozhushko, A.A. Radial Crater Growing Process in Different Materials with Shaped Charge Jets. *Propellants Explos., Pyrotech.* **1999**, *24*(6): 339-342.
[25] Rosenberg, Z.; Dekel, E. A Critical Examination of the Modified Bernoulli Equation Using Two-Dimensional Simulations of Long Rod Penetrators. *Int. J. Impact Eng.* **1994**, *15*(5): 711-720.
[26] Elshenawy, T.; Elbeih, A.; Li, Q.M. Influence of Target Strength on the Penetration Depth of Shaped Charge Jets Into RHA Targets. *Int. J. Mech. Sci.* **2018**, *136*: 234-242.
[27] Agu, H.O.; Hameed, A.; Appleby-Thomas, G. Application of Shell Jetting Analysis to Determine the Location of the Virtual Origin in Shaped Charges. *Int. J. Impact Eng.* **2018**, *122*: 175-181.
[28] Held, M. Behind Armor Effects at Shaped Charge Attacks. *Proc. 24th Int. Symp. Ballistics (ISB),* New Orleans, LA, USA, **2008**, pp. 1187-1198.
[29] Arabei, B.; Salibekov, S.; Levinskii, Y.V. On the Ignitability of Certain Powder Materials. *Powder Metall. Met. Ceram.* **1965**, *3*(3): 259-262.

[30] Aseltine, C.L. *Analytical Predictions of the Effect of Warhead Asymmetries on Shaped Charge Jets*. Army Ballistic Research Lab, Aberdeen Proving Ground MD, Report ARBRL-TR-02214, **1980**.

Received: July 5, 2019
Revised: July 8, 2021
First published online: July 16, 2021